Chapter 8
Cells and Subgrains. The Role of Cold Work

Abstract In almost all metals and alloys, dislocations are concentrated to narrow regions after plastic deformation that divide the material into cells or subgrains. The cell walls consist of tangles whereas the subgrains are surrounded by thin regular networks of dislocations. The cells are transferred to subgrains with increasing temperature. Although these substructures have been analyzed for many years, basic models of their development have only appeared recently. Models for substructures are presented for plastic deformation at constant stress and at constant strain rate. During straining the dislocations can move in opposite directions creating a polarized structure, where the possibility for recovery of dislocations is reduced. This can be expressed in term of a back stress. Its presence explains why creep curves at near ambient temperatures could have an appearance that is similar to that at elevated temperatures. It is also the basis for the effect of cold work on creep. The models can quantitatively describe why the creep rate can be reduced by up to six orders of magnitude for Cu after cold work.

8.1 General

Tangles of dislocations are formed in virtually all alloys during plastic deformation. With increasing strain the tangles form boundaries that divide the materials into micrometer sized cells or subgrains, Fig. 8.1. With increasing temperature and strain the boundaries become better developed and thinner. At high temperatures the boundaries consist of regular networks of dislocations, and are then referred to as subboundaries or subgrain boundaries. At lower temperatures the boundaries are made up of loose tangles that are called cell boundaries. Expressed in another way subgrains are formed in the creep range and cells in the work hardening range [1], although there is no sharp transition. For a definition of the work hardening and the creep range, see Sect. 3.4. Both cells and subgrains are referred to as substructure. In most materials the substructure is well developed already at modest strains. This means that the substructure can be observed in tensile and creep tests. However in

R. Sandström, *Basic Modeling and Theory of Creep of Metallic Materials*, Springer Series in Materials Science 339,
https://doi.org/10.1007/978-3-031-49507-6_8

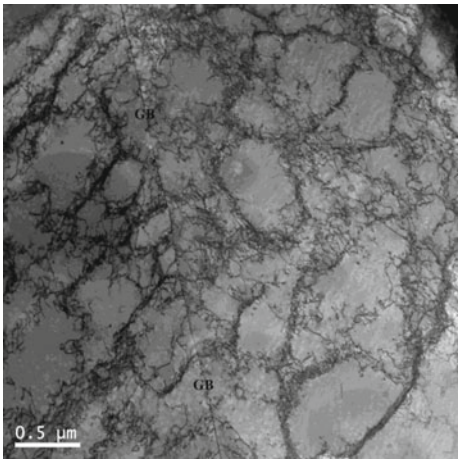

Fig. 8.1 Cell structure in Cu-OFP after 24% cold working [3]

some alloys, for example Al–Mg alloys, the development of substructure is delayed to higher strains [2].

There are excellent reviews on substructure formation in the literature [2, 4, 5]. Many results are similar for cells and subgrains so there is no need in general to make a clear distinction between them. For example, both the cell and subgrain sizes are related to the applied stress in the same way. One question that appeared early on was if the substructure contributed to the creep strength [5, 6]. In a number of investigations it has been shown that strength contribution from the dislocations in the subgrain interiors could account for the full creep strength in single phase alloys, see for example Orlova's paper [7]. However, with the event of Mughrabi's composite model where the subboundaries are considered as hard zones, it is clear that there are long range stresses from the subboundaries [8]. In the composite model, the strength is taken as a weighted average of the "hard" boundaries and the "soft" subgrain interiors. In a single phase alloy, the subgrain size is fully controlled by the applied stress and there is no way of varying the strength contribution from the subgrains [5]. However, the presence of particles can stabilize the subgrain size. In this way a major contribution to the creep strength from subgrains stabilized by $M_{23}C_6$ carbides is obtained in modern creep resistant 9–12% Cr steels [9].

There are many investigations on the formation of substructure but few of them are quantitative. Notable exceptions are work by Blum and Straub and coworkers who measured the development of the subgrain size during creep in martensitic steels [10–12]. These results could be combined with a basic model for the influence of particles on subgrain growth [13] to understand the long term behavior of 9–12% Cr steels [9].

Dislocations with burgers vectors $\mathbf{b}$ and $-\mathbf{b}$ in a slip system are moving in opposite directions in an applied stress field inside a cell. Dislocations with $\mathbf{b}$ and $-\mathbf{b}$ end up at opposite sides of the cells. If a cell boundary is considered, dislocations with $\mathbf{b}$ are found on one side of the boundary and those with $-\mathbf{b}$ on the other side. This means

that the cell boundaries become polarized. It has also the consequence that there is a boundary between the dislocations with **b** and $-\mathbf{b}$ and recovery of them cannot take place. These dislocations are also referred to as unbalanced because in the region with **b** dislocations there are no $-\mathbf{b}$ dislocations. This should be contrasted with balanced dislocations where dislocations with opposite burgers vectors are present. Models for the formation of substructure is presented in Sect. 8.2.

When unbalanced dislocations are present static recovery is slowed down since dislocation with opposite burgers vectors cannot meet and annihilate. The unbalanced dislocations are of importance for several properties. Modeling tertiary creep of copper has demonstrated that the recovery rate of the substructure gives a main contribution to the increasing strain rate [14]. This is likely to be the case for other ductile alloys as well. This will be further discussed in Sect. 12.4. Cold work can reduce the creep rate by many orders of magnitude. Taking balanced and unbalanced dislocations in the subgrain walls into account has made it possible to explain this quantitatively for copper [15]. The role of cold work is discussed in Sect. 8.3.

Most creep tests are performed at constant load. For example, when the creep rate is plotted versus stress, usually the engineering stress, i.e. the nominal stress is used, not the true stress. At high temperatures when the creep exponent is about 5 this is not so critical, but at lower temperatures in the power-law break down regime where the creep exponent can be 30–50, the difference between using the engineering and the true stress is huge, which can easily be demonstrated. It turned out for copper that the engineering stress is still the relevant quantity. It took many years to explain this feature, but by considering the role of the substructure it was possible, Sect. 8.4 [16].

8.2 Modeling of Subgrain Formation

8.2.1 The Stress from Dislocations

In previous chapters, the Taylor equation has been applied to describe the contribution to the strength from the dislocations, Eq. (2.28)

$$\sigma_{\text{disl}} = \alpha m_{\text{T}} G b \sqrt{\rho} \tag{8.1}$$

where α is constant, m_{T} the Taylor factor, G the shear modulus and b burgers vector. In the presence of substructure the relation has to be modified because the α value is different for dislocations in the cell boundary. This can be illustrated by an expression for α given by Kuhlmann-Wilsdorf [17]

$$\alpha_{\text{KW}} = \frac{(1 - \nu_{\text{P}}/2)}{6\pi(1 - \nu_{\text{P}})} \log \frac{R_{\text{CO}}}{b} \tag{8.2}$$

ν_P is Poisson's ratio and R_{CO} a cut-off ratio that is taken as the spacing between dislocations. This spacing is of the order of 10^{-7} m and 10^{-8} m in the cell interior and the cell boundaries respectively. This gives that α is close to a factor of 2 larger for dislocations in the cell interior than for dislocations in the cell boundaries. For this reason Eq. (8.1) is replaced by the following expression

$$\sigma_{\text{disl}} = \alpha m_T G b \sqrt{\rho_{\text{int}}} + \frac{1}{2} \alpha m_T G b \sqrt{\rho_{\text{bound}}} \tag{8.3}$$

where ρ_{int} is the dislocation density in the cell interior and ρ_{bound} the dislocation density in the cell boundaries. The value for α_{KW} will not be used in the present book, since there is an expression that is adapted to elevated temperatures, Eq. (3.17). As discussed in Sect. 8.1, there are many different results in the literature for the influence of boundary dislocations on the strength. Rather than trying to select between the various experimental results, a direct derivation has been chosen.

There is a well-established relation between the cell or subgrain size d_{sub} and the stress

$$d_{\text{sub}} = \frac{K_{\text{sub}} G b}{\sigma_{\text{disl}}} \tag{8.4}$$

K_{sub} is a dimensionless constant that typically takes values in the interval 10 to 20. The first ones to propose an equation of this form were Staker and Holt [18]. It is assumed that it is the dislocation stress that is used in Eq. (8.4) [17]. Eq. (8.4) was already given in Sect. 2.4. It has been suggested that Eq. (8.4) is general and does not only apply to stationary conditions [19]. There are two well-known derivations of Eq. (8.4) in the literature. In the first one a spinodal decomposition of a set of parallel screw dislocations was considered [20]. In the second one the energy of a substructure was assumed to be the sum of the dislocation line energy and the dislocation cell stresses. By minimizing the sum of these two contributions, Eq. (8.4) was obtained [17].

The distance between dislocations in the cell walls which is referred to as the dislocation separation can be estimated in the following way. For the sake of argument, the cell walls are assumed to consist of one layer of μ sets of dislocations and cells arranged as packed cubes. The density of boundary dislocations is then given by

$$\rho_{\text{bnd}} = \frac{3\mu d_{\text{sub}}^2}{d_{\text{sub}}^3 l_{\text{sep}}} \tag{8.5}$$

where l_{sep} is the dislocation separation. Each corner in the arrangements of the cube substructure is associated with three cube sides and that is the reason for the factor 3 in Eq. (8.5). The density is taken as the average over the volume of each cell d_{sub}^3. Equation (8.5) will be used below to obtain an estimate for the dislocation separation.

8.2.2 Formation of Subgrains During Creep

In most materials well-formed subgrains are present in the secondary stage. This means that the subgrains are created during primary creep. There are exceptions. In Al-Mg alloys at around 300 °C, subgrains are not formed until a strain of about 1 [2]. In addition, in some stainless steels a homogeneous dislocation structure appears under certain conditions. For 17Cr12Ni2Mo subgrains appeared at 704 °C but not at 593 °C [21]. For 17Cr12Ni2MoN no subgrains were present at higher N content [22]. A possible qualitative explanation to these observations is that the stacking fault energy γ_{SFE} plays a role and that the subgrain formation increases with the value of γ_{SFE}. For 17Cr12Ni2Mo there is a dramatic increase in γ_{SFE} with temperature [23], which could explain the observations in [21]. The results of the influence of N on γ_{SFE} in the literature are far from unanimous but a recent analysis of existing data [24] suggests that N reduces γ_{SFE} and this could be a reason for the findings in [22]. For Al–Mg, the value of γ_{SFE} is considerably lower than for Al, but if this is of importance for the substructure formation is uncertain.

The normal case where subgrains are present in the secondary stage will now be considered. The changes of the substructure have been quantitatively studied for an Al5Zn alloy at a temperature of 250 °C and an applied stress of 16 MPa. The study was performed by Blum and co-workers. The original papers are not readily available anymore, but fortunately the results are reproduced in other sources [2, 25]. In Sect. 4.3, a model for primary creep is presented. The creep rate is given by Eqs. (4.3) and (4.9)

$$\dot{\varepsilon} = h(2(\sigma - \sigma_{\mathrm{i}}) - \sigma_{\mathrm{disl}}) \tag{8.6}$$

where

$$h(\sigma) = 2\tau_{\mathrm{L}} M(T,\sigma) \frac{\sigma^3}{(\alpha m_{\mathrm{T}} G b)^3} \Big/ \left(\frac{m_{\mathrm{T}}}{b c_L} - \omega \frac{\sigma}{\alpha m_{\mathrm{T}} G b} \right) \tag{8.7}$$

In Eq. (8.6), there is an effective stress that controls the creep rate in the primary stage

$$\sigma_{\mathrm{eff}} = 2(\sigma - \sigma_{\mathrm{i}}) - \sigma_{\mathrm{disl}} \tag{8.8}$$

As can be seen from Eq. (4.10), there is a contribution from solid solution hardening. For Al5Zn, this contribution comes from the Zn content. The linear misfit for Zn in Al is −0.02. The drag stress from the Zn content is given by (Eq. (6.20))

$$\sigma_i^{\mathrm{drag}} = \frac{v_{\mathrm{climb}} c_{i0} \beta^2}{b D_i k_{\mathrm{B}} T} I(z_0) \tag{8.9}$$

The resulting value of σ_i is 4.6 MPa. For $h(\sigma)$ values for Al are used, see Sect. 2.7. The creep strain and the strain rate are illustrated Fig. 8.2.

The creep rate versus strain follows the ϕ-model, Sect. 4.2, although the slope is not quite the same in the experiments and the model.

Since the effective stress controls the primary creep rate, it is natural to assume that it also governs the subgrain size. By applying Eq. (8.8) in Eq. (8.4) a simple model is obtained. The findings are shown in Fig. 8.3a.

The variation of the dislocation density with strain can also be derived with the help of Eq. (4.5). The result is given in Fig. 8.3b. Once the dislocation density is known, the dislocation separation in the subgrain boundaries can be obtained with the help of Eq. (8.5). It is assumed that most of the dislocations are located in the boundaries. The result is demonstrated in Fig. 8.4.

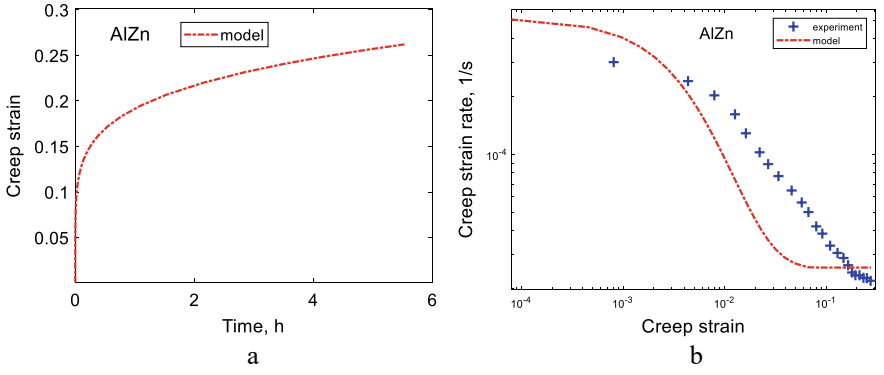

Fig. 8.2 Creep strain versus time **a** and creep rate versus strain **b** for Al5Zn at 250 °C and 16 MPa. Experimental data from [2, 25]. Redrawn from [26] with permission of MDPI

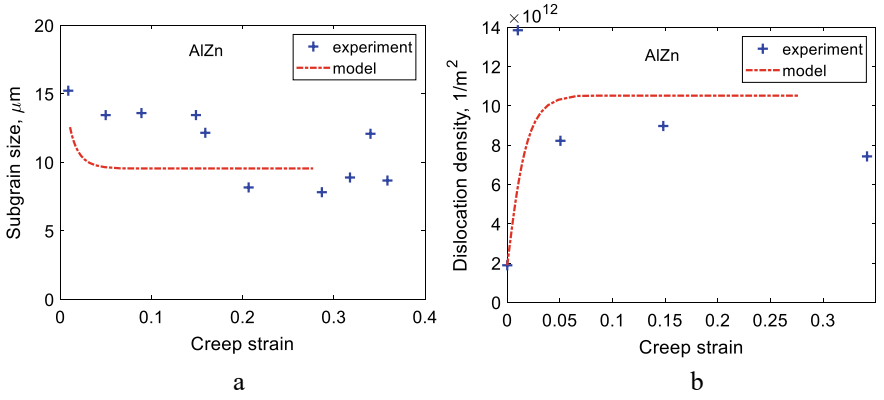

Fig. 8.3 Subgrain size **a** and dislocation density **b** versus strain for Al5Zn at 250 °C and 16 MPa. Experimental data from [2, 25]. Redrawn from [26] with permission of MDPI

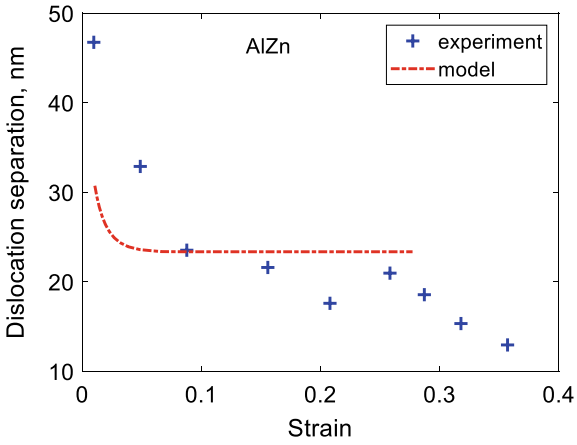

Fig. 8.4 Dislocation separation in the subgrain boundaries versus strain for Al5Zn at 250 °C and 16 MPa. Experimental data from [2, 25]. Redrawn from [26] with permission of MDPI

It is clear that the model presented here can predict the general behavior of the subgrain formation in Figs. 8.3 and 8.4 although the details are not fully accurate.

8.2.3 Cell Formation at Constant Strain Rate

Dislocation cells are formed in virtually all alloys during tensile and compression testing at ambient temperatures. A brief survey is given by Koneva et al. [27]. In the same way as during creep, the cell diameter decreases with increasing strain. They summarize findings that the cell diameter is proportional to the inverse of the square root of the dislocation density.

$$d_{\text{sub}} = K_{\text{rho}} \rho^{-1/2} \tag{8.10}$$

This is consistent with Eq. (8.4). This is seen by combining Eqs. (8.3) and (8.4) with (8.10)

$$K_{\text{rho}} = \frac{K_{\text{sub}} \mu_{\text{sub}}}{\alpha m_{\text{T}}} \tag{8.11}$$

where $\mu_{\text{sub}} = 1$ and 2 for dislocation densities in the subgrain interior and walls respectively. A value of $K_{\text{rho}} = 15$ was found for Cu which is in reasonable agreement with $K_{\text{sub}} = 10$, since $\alpha \approx 0.19$ and $m_{\text{T}} \approx 3.1$. The location of dislocation in cell interiors or boundaries was not specified. Their results for K_{rho} for Cu–Al (2–5) and for Cu–Mn (2–5) illustrate that K_{rho} can be significantly smaller for alloys in comparison to pure metals. In [27] early investigations for K_{rho} are also referenced but these results are difficult to match to K_{sub} values.

Subgrain boundaries have essentially zero width in particular at high temperatures. Cell walls on the other hand have a significant width w_{cell}. This means that Eq. (8.5) must be replaced by

$$\rho_{\text{bnd}} = \frac{3\mu w_{\text{cell}}}{d_{\text{sub}} l_{\text{sep}}^2} \tag{8.12}$$

In Eq. (8.12), the separation distance between dislocations is assumed to be the same in the boundary plane and perpendicular to the plane. In the boundary several types of dislocations must be taken into account [15]. This will be explained in detail in Sect. 8.2.3, where the equations for the dislocation densities will be given. Using these equations the developments of dislocation densities and the corresponding dislocation stress, Eq. (8.3), can be computed. Once the dislocation stress is known, the cell size can be obtained with the help of Eq. (8.4). The variation of the cell size as a function of strain is illustrated in Fig. 8.5. The cell diameter decreases with increasing strain and tends towards a stationary value at larger strains.

In addition to the overall dislocation density in the boundary ρ_{bnd}, there is a formation of dislocation locks that are believed to create the stability of the boundary. The density of the locks is designated ρ_{lock}. Following [15] the cell wall width is related to the lock density

$$w_{\text{cell}} = \frac{1}{l_{\text{sep}} \rho_{\text{lock}}} \tag{8.13}$$

If Eqs. (8.12) and (8.13) are combined, expressions for the dislocation separation and wall width in terms of the dislocation densities are obtained

$$l_{\text{sep}} = \left(\frac{3\mu}{d_{\text{sub}} \rho_{\text{bnd}} \rho_{\text{lock}}} \right)^{1/3} \tag{8.14}$$

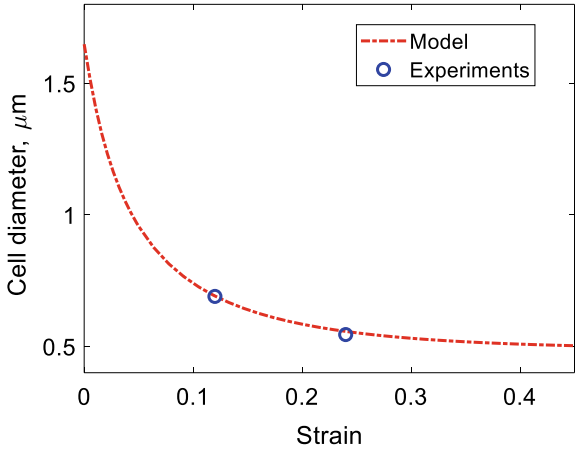

Fig. 8.5 Cell diameters as a function of strain for Cu-OFP at 75 °C and 1×10^{-5} 1/s [15]. Experimental data from [3]. Redrawn from [15] with permission of Elsevier

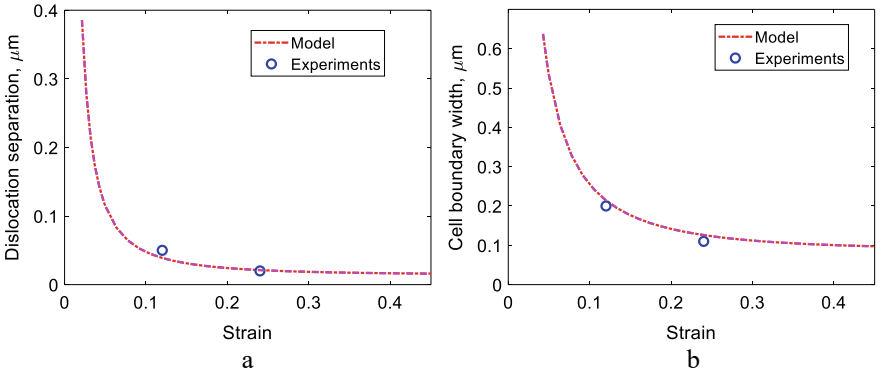

Fig. 8.6 **a** Dislocation separation in the cell boundaries and **b** cell boundary width as a function of strain for Cu-OFP at 75 °C and 1×10^{-5} 1/s [15]. Redrawn from [15] with permission of Elsevier

$$w_{\text{cell}} = \left(\frac{d_{\text{sub}} \rho_{\text{bnd}}}{3\mu\rho_{\text{lock}}^2} \right)^{1/3} \tag{8.15}$$

Equations (8.14) and (8.15) are compared to experimental data in Fig. 8.6.

In the same way as for the cell size, the dislocation separation and cell boundary width decrease with strain. The variation of the dislocation separation and cell boundary width with strain is more rapid than for the cell size. These results are not consistent with those of Koneva et al., who suggest a constant ratio between the cell boundary width and the cell diameter.

In a test series for 18Cr8Ni austenitic stainless at 865 °C, the formation of subgrains as a function of strain at constant strain rate is studied in [2]. In the same way as for Al5Zn and Cu-OFP above, it is demonstrated that the subgrain size and dislocation separation in subgrain walls decrease and tend to stationary values with increasing strain. The dislocation density rapidly increases with strain and also levels off to a stationary value. Since the variation of the stress with strain can be predicted, it was thought that the results should be possible to model. Unfortunately, the published stress strain curve is not consistent with the creep models.

8.3 Influence of Cold Work on the Creep Rate

The influence of cold deformation on the creep rate and creep rupture is a classical problem. During primary creep of annealed material, the dislocation density is normally raised from a low value to a stationary one when the secondary stage is reached. This is a direct outcome of the creep recovery theory and it is well described by the basic dislocation equation used in this book, Eq. (4.5). On the other hand for a cold deformed material, the initial dislocation density is high.

If Eq. (4.5) is applied, the dislocation density would be reduced during primary creep and the same stationary dislocation density as for an annealed material would be found and no effect of the cold deformation would remain. This is in direct at variance with observations for example for fcc alloys. For a number of austenitic stainless steels the creep strength can be increased significantly [28–31]. A review is given in [32]. If the temperature is too high or the strain is too large the effect of cold work disappears. The reason is that the dislocation structure is not sufficiently stable under such conditions and recrystallization may appear.

In this section the influence of cold work on the creep of Cu-OFP will be analyzed. Results for creep rupture data are shown in Fig. 8.7.

Values for 0, 12 and 24% cold work are compared. It is evident that the cold work has a dramatic effect on the rupture time. For 12% cold work the rupture time is increased by more than three orders of magnitude. For 24% cold work the rupture time is raised by six orders of magnitude. This effect is only observed if the cold work is performed in tension. If the cold work is in compression only quite a small increase in the rupture time is found. The creep testing was carried out in tension. Thus if the deformation direction is reversed between the cold work and creep testing only a limited effect is observed.

With increasing cold deformation, the creep ductility is practically always reduced. This is clearly found for Cu-OFP, Fig. 8.8.

For Cu-OFP without cold work the rupture elongation is typically quite high, above 40%. For 12% cold deformation in tension the rupture elongation is still high, 30% and above. For 24% cold deformation, the rupture elongation is a little bit above 10%. It is interesting to note that the creep ductility of Cu-OFP deformed in compression is low in spite of the small increase in the rupture time.

It has now been found that the role of the substructure must be taken into account to understand the influence of cold working [15]. This has also been suggested in the past but without any basic analysis that could predict the magnitude of the effect [4, 33]. As described in Sects. 8.1 and 8.2 a cell structure is formed in practically all alloys

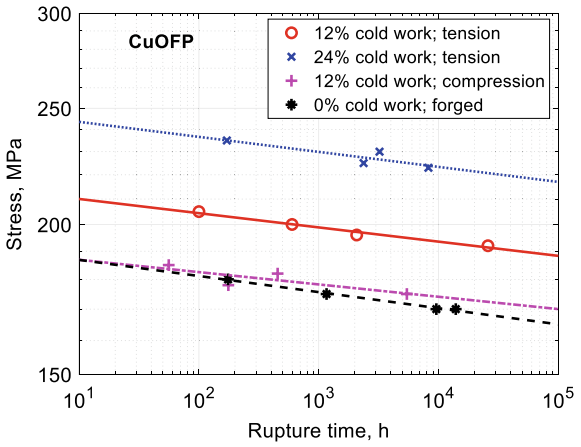

Fig. 8.7 Stress versus rupture time for 12 and 24% cold deformed Cu-OFP at 75 °C. For comparison data for material without cold deformation is included. The lines are fitted to the experimental data to illustrate the influence of rupture time. Experimental data from [3]. Redrawn from [15] with permission of Elsevier

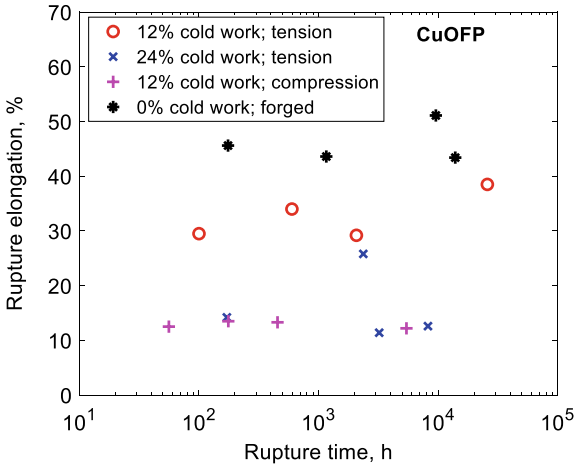

Fig. 8.8 Rupture elongation versus rupture time for 12 and 24% cold deformed Cu-OFP at 75 °C. For comparison data for material without cold deformation is included. Experimental data from [3]. Redrawn from [26] with permission of MDPI

during deformation at ambient temperatures. A large fraction of the dislocations moves to the cell boundaries and in this way they create the cell structure. During the deformation all dislocations do not behave in the same way. Dislocations with opposite burgers vectors move in opposite directions in a given stress field. This can be seen from the Peach-Koehler formula for the force **F** on a dislocation with direction ξ and burgers vector **b**

$$\mathbf{F} = (\mathbf{b}\sigma) \times \boldsymbol{\xi} \tag{8.16}$$

If the direction of the burgers vector is changed to the opposite one ($-\mathbf{b}$), this is the same as changing the sign of the burgers vector. For this reason, burgers vectors of opposite directions will also be referred to as burgers vectors of opposite signs. From Eq. (8.16), it can be seen that if the direction of the burgers vector is changed to the opposite one, the sign and the direction of the force is also changed. Dislocations of opposite signs on the same glide plane move to different ends of the cell. With opposite signs at different ends of the cell, the dislocations are said to be polarized. Not all dislocations are polarized. It is assumed that the outer layers of the boundaries are polarized.

The polarization of dislocations has a pronounced effect on the recovery. Since dislocations with opposite burgers vectors cannot be found amongst polarized dislocations, static recovery is not possible. Polarized dislocations are referred to as unbalanced since dislocations with opposite burgers vector are not present. For unpolarized dislocations, dislocations with opposite burgers vectors can be found and they are therefore referred to as balanced.

In the model for the development of the cell structure, the following dislocation densities in the cell boundaries are taken into account: balanced dislocation density ρ_{bnd}, the unbalanced dislocation density ρ_{bnde}, and the density of the locks ρ_{lock} [15]. Most of the dislocations are in the boundaries, and the content in the cell interiors is

neglected. The equation for the balanced dislocation density ρ_{bnd} is almost identical to Eq. (2.17)

$$\frac{d\rho_{\text{bnd}}}{d\varepsilon} = k_{\text{bnd}} \frac{m\rho_{\text{bnd}}^{1/2}}{bc_L} - \omega\rho_{\text{bnd}} - 2\tau_{\text{L}} M\rho_{\text{bnd}}^2/\dot{\varepsilon} \tag{8.17}$$

Work hardening, dynamic recovery and static recovery are considered. The only difference is the introduction of the factor k_{bnd}. It takes into account since Eq. (8.3) is modified in comparison to the ordinary version of the Taylor equation. For the unbalanced content ρ_{bnde}, the equation corresponding to (8.17) is

$$\frac{d\rho_{\text{bnde}}}{d\varepsilon} = k_{\text{bnde}} \frac{m(\rho_{\text{bnd}}^{1/2} + \rho_{\text{bnde}}^{1/2})}{bc_L} - \omega\rho_{\text{bnde}} \tag{8.18}$$

There are two significant differences between (8.17) and (8.18). There is no static recovery term in Eq. (8.18). Unbalanced dislocations cannot annihilate by combining with dislocations of opposite signs, since such dislocations are not present. The other difference is that both balanced and unbalanced contribute to the generation of the unbalanced content since both types move across the cell interiors.

The traditional view is that dynamic recovery is due to dislocations coming sufficiently close that they can combine with dislocations of opposite sign and annihilate [34]. This assumption tends to overestimate the recovery rate, see Sect. 2.3.2. In addition, the mechanisms for dynamic and static recovery would be similar although their temperature and time dependencies are quite different. Argon has instead suggested that the dynamic recovery is due to the interaction between dislocations generated during work hardening and the cell boundaries [35]. It is known experimentally that spurting dislocations are moving a distance of about three cell diameters [36] and consequently they will pass through more than one cell boundary. During this passage boundary dislocations will be removed. When the dislocations hit the boundaries low energy configurations will be formed and this is part of the dynamic recovery process. Some of these low energy configurations are locks that are dominated by Cottrell-Lomer locks. They are created when partial dislocations cross. The formation of locks are assumed to be controlled by the following equation

$$\frac{d\rho_{\text{lock}}}{d\varepsilon} = k_{\text{lock}}\omega(\rho_{\text{bnd}} + \rho_{\text{bnde}}) - \omega\rho_{\text{lock}} - 2\tau_{\text{L}} M\rho_{\text{lock}}^2/\dot{\varepsilon} \tag{8.19}$$

This equation describes how both balanced and unbalanced dislocations contribute to the formation of locks. Dynamic recovery influences the number of locks since spurting dislocations passing through the boundaries remove locks. The locks can also be eliminated by static recovery since this process reduces the energy even for complex dislocation configurations.

In Sect. 3.3, experimental stress strain curves for Cu-OFP were accurately reproduced using Eq. (2.17) assuming a homogenous distribution of dislocations. If now

the dislocations are considered to be located in the cell boundaries and Eqs. (8.17)–(8.19) are used, the stress should be computed with the help of Eq. (8.3) with ρ_{bound} equal to the sum of ρ_{bnd}, ρ_{bnde} and ρ_{lock}. The results for the stress strain curves should be the same. With $k_{bnd} = \sqrt{2}$ and $k_{bnde} = \sqrt{2}$ this is the case. The value of k_{lock} should be considerably smaller than the value for k_{bnd}. A value of $k_{lock} = 0.1$ has been assumed. With Eq. (8.14), this gives a value for the separation distance of the dislocations in the cell walls of about 20 nm that is in accordance with experiments for several materials, see Sect. 8.2. The selection of k_{lock} also affects the values k_{bnd} and k_{bnde}. Values $k_{bnd} = 1.7$, $k_{bnde} = 0.2$ and $k_{lock} = 0.1$ reproduce the stress strain curves [15].

The results for the influence of cold work in Fig. 8.7 will now be analyzed. 12% and 24% cold deformation at ambient temperature gives stresses of 154 and 191 MPa, respectively. Assuming the dislocations are located in cell boundaries in agreement with observations [3], and using the modified Taylor Eq. (8.3), this gives total densities of dislocations in the cell walls of 8.7×10^{14} and 1.5×10^{15} $1/m^2$. The development of the dislocation densities according to in Eqs. (8.17)–(8.19) is shown in Fig. 8.9. In this case the balanced dislocations dominate the total content. It should be emphasized that the stresses from the cold work are much higher than even the dramatic increase in creep strength demonstrated in Fig. 8.7. Extensive recovery is taken place but not to such an extent that the stationary state for annealed material is reached.

The key to understanding the influence of cold work is the unbalanced dislocation density ρ_{bnde} that is not exposed to static recovery. It is assumed to give rise to a back stress that reduces the creep rate

$$\sigma_{back} = \frac{m\alpha Gb}{2}\sqrt{\rho_{bnde}} \tag{8.20}$$

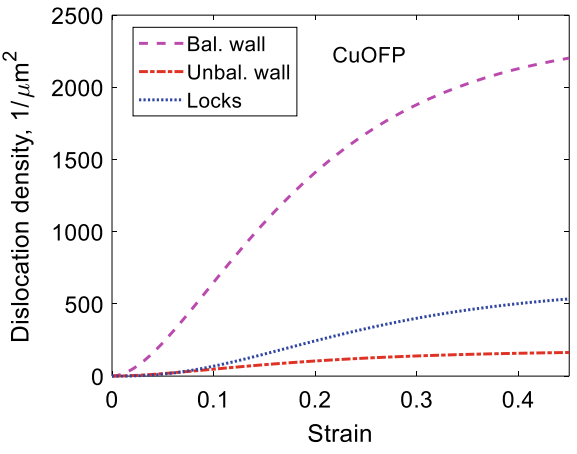

Fig. 8.9 Densities of balanced, unbalanced and lock dislocations in the cell boundaries as a function of strain for Cu-OFP. Redrawn from [15] with permission of Elsevier

If the secondary creep rate for undeformed material is $\dot{\varepsilon}_{\text{sec}}(\sigma)$, the corresponding value for cold worked material is

$$\dot{\varepsilon}_{\text{sec CW}}(\sigma) = \dot{\varepsilon}_{\text{sec}}(\sigma - \sigma_{\text{back}}) \tag{8.21}$$

where σ is the applied creep stress. It might be thought that the back stress could be measured in a stress drop test by reducing the applied stress until the creep rate vanishes. However, this is not possible. The stress drop is in general based on the assumption that the dislocation structure is essentially unchanged after the reduction in stress. With dislocation dynamics it has been demonstrated that the dislocation structure is adapted to the new stress level within milliseconds [37]. This applies both to the dislocations in the cell interior and in the cell walls. On the other hand it takes a longer time before the cell size corresponds to the new stress level. Thus the dislocation structure after a stress drop neither represents the old stress level nor the new one. Back stresses can be quite useful in modeling, but to measure them would require quite a sophisticated analysis to interpret the results.

The stress dependence of the secondary creep rate according to Eq. (4.3) is given by

$$h(\sigma) = 2\tau_{\text{L}} M(T,\sigma)\frac{\sigma^3}{(\alpha m_{\text{T}} Gb)^3} \Big/ \left(\frac{m_{\text{T}}}{bc_L} - \omega\frac{\sigma}{\alpha m_{\text{T}} Gb}\right) \tag{8.22}$$

which is inserted into Eq. (8.21)

$$\dot{\varepsilon}_{\text{sec CW}}(\sigma) = h(\sigma - \sigma_{\text{back}}) \tag{8.23}$$

To handle primary creep, Eqs. (4.6) and (4.7) are applied

$$\sigma_{\text{prim}} = \sigma_{\text{disl sec}} - \sigma_{\text{disl}} \tag{8.24}$$

$$\dot{\varepsilon} = h(\sigma + \sigma_{\text{disl sec}} - \sigma_{\text{disl}} - \sigma_{\text{back}}) \tag{8.25}$$

σ_{disl} is the stress created by the dislocations. In the secondary stage this stress takes the value σ_{dislsec}. Thus, in the secondary stage, Eq. (8.25) is identical to Eq. (8.21).

The use of Eq. (8.25) with no cold work present has been illustrated for Cu-OFP in Fig. 4.10. It was demonstrated that the primary creep could be well reproduced and that both the experimental and the model results followed the ϕ-model.

Two examples of creep-strain curves for 12% cold-work Cu-OFP are shown in Fig. 8.10.

Both the experimental and model curves show distinct primary and secondary stages. The model exaggerates somewhat the size of the primary stage and reaches the secondary stage too soon. The model accurately reproduces the creep rate in the secondary stage in spite of the fact that the creep rate is three orders of magnitude lower than without cold work. This would not be possible unless the recovery rate

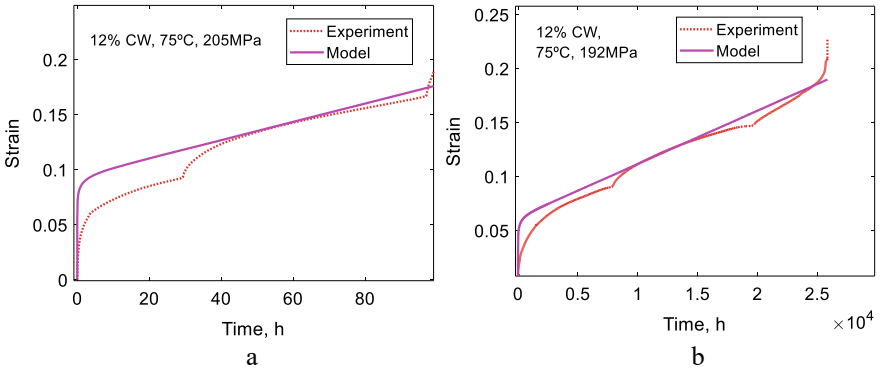

Fig. 8.10 Creep strain versus time for 12% cold worked Cu-OFP at 75 °C, **a** 205 MPa and **b** 192 MPa. Model results from integration of Eq. (8.25). Redrawn from [15] with permission of Elsevier

of the unbalanced dislocations would be much lower than for the other types of dislocations. The amount of tertiary creep is very limited in the experimental data and the tertiary stage appears late in the test. It is probably caused by necking [14]. Since necking is not taken into account in the creep model, it is then natural that tertiary creep is absent in the model curves.

For one of the cases in Fig. 8.10, the creep rate as a function of time is given in Fig. 8.11.

In the same way as in Fig. 4.10b the experiment and the model obeys the ϕ-model at least approximately. The drop in strain rate with increasing time is however much more dramatic in Fig. 8.11 in comparison to Fig. 4.10b.

Creep strain curves for 24% cold deformed Cu-OFP are illustrated in Fig. 8.12.

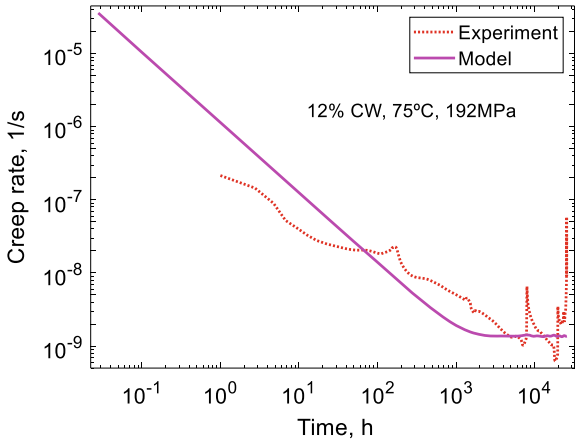

Fig. 8.11 Creep strain rate versus time for 12% cold-work Cu-OFP at 75 °C and 192 MPa. Model results from Eq. (8.25). Redrawn from [15] with permission of Elsevier

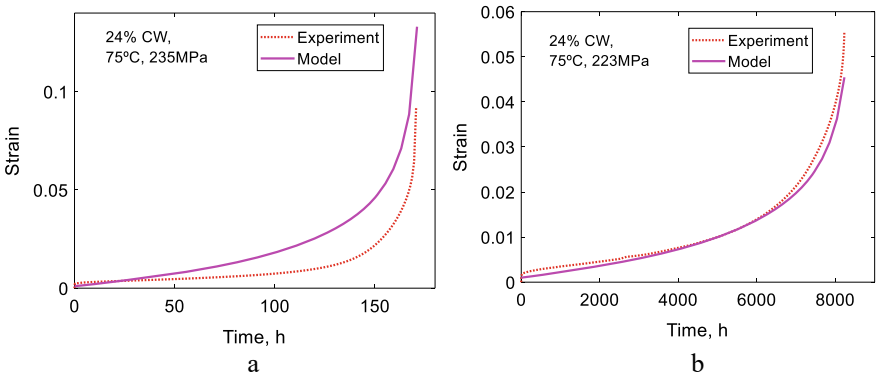

Fig. 8.12 Creep strain versus time for 24% cold-work Cu-OFP at 75 °C, **a** 235 MPa and **b** 223 MPa. Model results from integration of Eq. (8.25). Redrawn from [15] with permission of Elsevier

It is immediately evident that that creep strain curves for 24% cold deformed material are very different from those of 12% cold deformed. In Fig. 8.12, primary and secondary creep is only present to a limited extent and tertiary creep is totally dominating. It is striking that the model can reproduce the creep strain curves also in this case. The cell sizes are smaller, the boundaries are narrower and the dislocations in the walls are closer for 24% cold deformed materials in comparison to 12% cold deformed, see Figs. 8.5 and 8.6. It is believed that the continuously increasing creep rate is due to enhanced recovery [14]. Tertiary creep will be further discussed in Chap. 12.

It can be concluded that by taking the back stress from the unbalanced dislocations into account, Eq. (8.12), the main features for cold deformed Cu-OFP can be well described. Thus, the reduction of the creep rate by three and six orders of magnitude for 12 and 24% can be modeled. The whole creep curves can be reproduced in a reasonable way. In the argument above the model was analyzed for primary and secondary creep. It will be seen in Chap. 12 on tertiary creep that Eq. (8.25) is also valid for tertiary creep. This is also clearly demonstrated in Fig. 8.12.

In the analysis above it has been assumed that the substructure is stabilized by the presence of unbalanced dislocation. An alternative way is to use particles to stabilize the substructure. This is extensively utilized for modern 9%Cr steels [38]. For the influence of cold work on the creep rate of austenitic stainless steels it has been suggested that particles can lock the substructure and prevent that the effect of cold work is lost [28, 29]. However, no detailed analysis of the role of the particles has been performed.

8.4 Formation of a Dislocation Back Stress

Cu-OFP close to ambient temperatures show creep curves that have the same appearance as at much higher temperatures with distinct primary, secondary and tertiary creep. One example is given in Fig. 8.13.

The cusp on the experimental curve is due to the necessity to reload the creep machine. Thus, the creep curves have many characteristics in common with typical creep curves at higher temperatures at about half the melting point. However, there is one aspect that is different. It is in general assumed that the true creep rate is constant in the secondary stage. This is frequently a starting point in stress analysis with finite element programs. To check if that is the case for the creep curve in Fig. 8.13, it is assumed for simplicity that the creep rate can be described with a Norton equation

$$\frac{d\varepsilon}{dt} = A_0(\sigma_0 e^{\varepsilon})^{n_N} \tag{8.26}$$

where A_0 is a constant and σ_0 is the nominal applied stress. The stress exponent n_N is about 70 for the case in Fig. 8.13. The factor e^{ε} takes into account the increase in the true stress when the specimen cross section is reduced during straining. A_0 is chosen so the Norton expression crosses the experimental at 600 h, which is about half the rupture time. Equation (8.26) is now integrated starting with $\varepsilon_0 = 0.17$ to simulate the influence of primary creep. The result is included in Fig. 8.13. It is obvious that Eq. (8.26) cannot represent the creep curve in Fig. 8.13. This conclusion is in no way affected by the choice of parameter values in Eq. (8.26).

The creep exponent $\exp(n_N\ \varepsilon)$ in Eq. (8.26) has a dramatic effect on the strain rate giving a creep curve with rapidly increasing slope that is fully inconsistent with observations. The effect is in fact quite large. For example, for $\varepsilon = 0.1$, $\exp(n_N\ \varepsilon)$ is equal to 1100. This enormous increase has never been observed in creep curves and

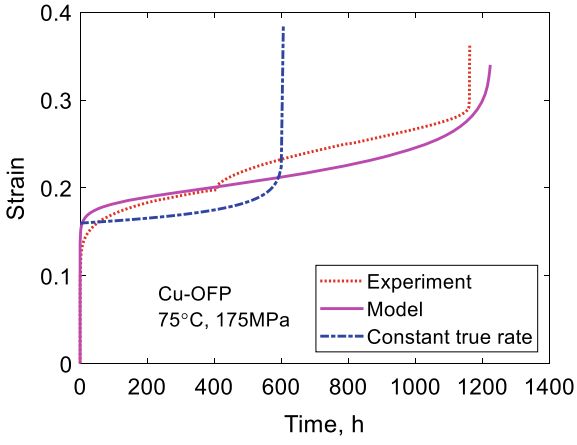

Fig. 8.13 Creep strain versus time for Cu-OFP at 75 °C and 175 MPa. Forged material. The model curve is derived with Eq. (8.25). Redrawn from [16] with permission of Elsevier

one can conclude that the simple assumption of a constant true strain is strongly at variance with observations.

Instead there must be a back stress that prevents the rapid increase in the strain rate. The back stress must be built up in the dislocation structure

$$\sigma_{\text{back}} = \sigma_{\text{disl}} - \sigma_0 \tag{8.27}$$

σ_{disl} is given by Eq. (8.3). σ_0 is again the nominal applied stress. It is related to the true applied stress σ as

$$\sigma = \sigma_0 \exp(\varepsilon) \tag{8.28}$$

The stress σ_{creep} that drives the creep deformation is given by

$$\sigma_{\text{creep}} = \sigma - \sigma_{\text{back}} = \sigma + \sigma_0 - \sigma_{\text{disl}} \tag{8.29}$$

In the second equality, Eq. (8.27) has been applied. Thus by applying Eq. (4.6), the creep rate is given by

$$\dot{\varepsilon} = h(\sigma + \sigma_0 - \sigma_{\text{disl}}) \tag{8.30}$$

It is interesting to compare this equation with the simplified version in Eq. (4.9). In Eq. (4.9), the applied stress is the nominal one but at the same time the full impact of substructure on σ_{disl} is not included. For primary and secondary creep these differences are not very important. However, Eq. (4.9) cannot describe tertiary creep contrary to Eq. (8.30), which will be explained now.

The development of the balanced and unbalanced dislocation densities ρ_{bnd} and ρ_{bnde} for the case in Fig. 8.13 is illustrated in Fig. 8.14. Equations (8.17) and (8.18) are used. The small contribution from ρ_{lock} is neglected in this case. Since the relation between ρ_{bnd} and ρ_{bnde} is not known, the relation between k_{bnd} and k_{bnde} cannot be determined. It is assumed that $k_{\text{bnd}} = k_{\text{bnde}}$ with a value of $\sqrt{2}$ that reproduces the results of Sect. 4.3.

As can be seen from Fig. 8.14a, the balanced dislocation density reaches an approximately constant value in the secondary stage whereas the unbalanced content increases continuously even during the secondary stage. The implication for the dislocation stresses is shown in Fig. 8.14b. The total stress from the balanced and the unbalanced dislocation stresses are marked as 'all'. This total dislocation stress matches the true applied stress σ in the secondary stage. This is the reason why the creep rate does not increase in an uncontrolled way. This balance is possible due to the increase in the unbalanced stress. The difference between the starting value of the applied stress of 150 MPa and the test stress of 175 MPa is the value of the yield strength. With increasing strain the total dislocation stress cannot match the true applied stress anymore. Then the tertiary stage is reached and the creep rate increases.

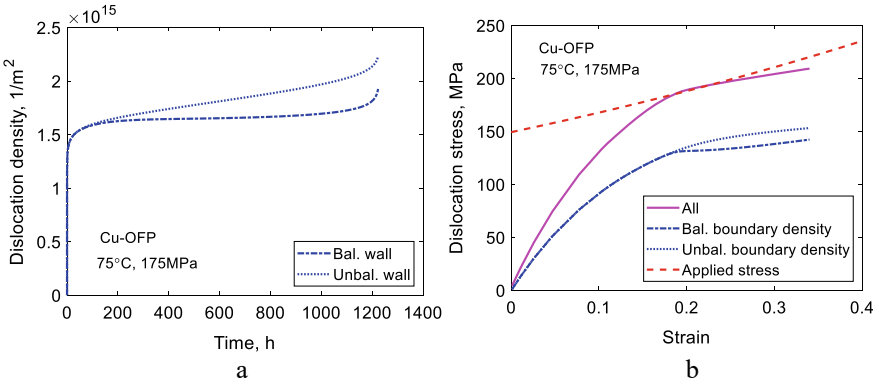

Fig. 8.14 Model results for the same case as in Fig. 8.13 (Cu-OFP at 75 °C and 175 MPa). **a** Dislocation densities versus time; **b** dislocation stresses versus strain. Redrawn from [16] with permission of Elsevier

It can be seen from Fig. 8.13 that tertiary creep is reasonably well represented. This can also be demonstrated by plotting the strain rate as a function of time, Fig. 8.15.

Although the cusps in the experimental data do not make a detailed comparison possible, it is evident that the overall picture reproduces both the primary and tertiary stages in a good way.

It can be concluded that the presence of back stress from the unbalanced dislocations, prevents the creep rate from increasing in an uncontrolled way that would be suggested if a constant true strain rate in the secondary would be assumed. In addition, the introduction of this back stress makes it possible to model tertiary creep.

Also stress strain curves seem to be affected by the back stress. One example is illustrated in Fig. 8.16. A stress strain curve for 15% cold worked Cu-OFP is shown. A model curve using Eqs. (8.3), (8.17) and (8.18) is also included in Fig. 8.16a.

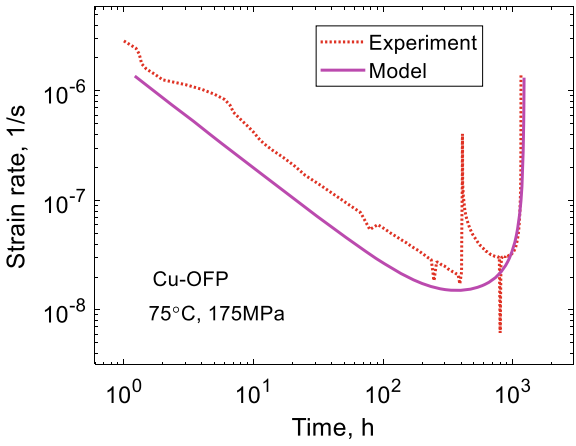

Fig. 8.15 Creep rate versus time for the curve in Fig. 8.13 (Cu-OFP, 75 °C and 175 MPa). Forged material. Redrawn from [16] with permission of Elsevier

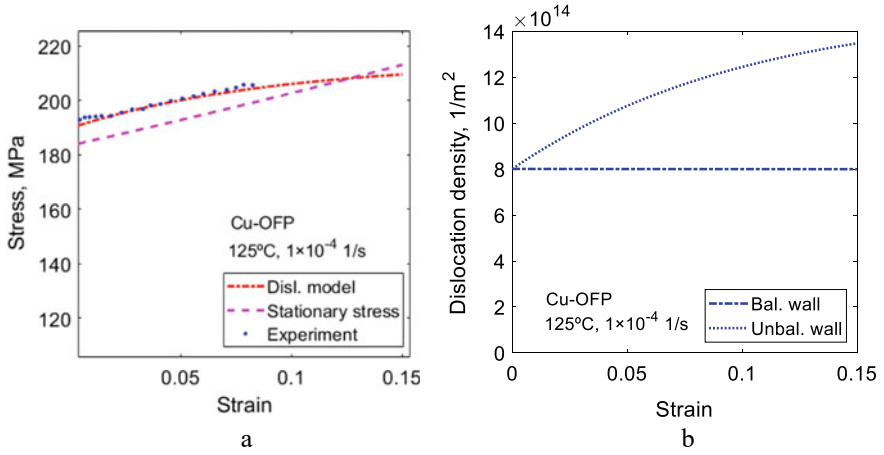

Fig. 8.16 Stress strain curve for 15% cold worked Cu-OFP at 125 °C and 1×10^{-4} 1/s; **a** the experimental curve is compared to modeling results with Eqs. (8.3), (8.17) and (8.18) for balanced and unbalanced boundary dislocations; **b** balanced and unbalanced boundary (wall) dislocation density. Experiments from [39]. Redrawn from [16] with permission of Elsevier

It is assumed that the stress strain relations are controlled by the same equations as the creep curves in the same way as in other parts of this book. This means that the stress level at higher strains should correspond to the stationary stress in a creep test. This stress is given by

$$\sigma_{\text{stat}} = \sigma_{\text{stat0}} e^{\varepsilon} \tag{8.31}$$

where σ_{stat0} and σ_{stat} are the nominal and the true stationary stress that give the same strain rate as in the stress strain curve (1×10^{-4} 1/s at 125 °C). The stationary stress is not identical to the stress strain curve but it is very close to supporting the assumed principle.

The strain dependence of the dislocation densities is given in Fig. 8.16b. The balanced and unbalanced dislocation densities are assumed to be the same at zero strain. Using these assumptions, the values of k_{bnd} and k_{bnde} can be determined, see [16] for details. It can be seen from Fig. 8.16b that the unbalanced dislocation density increases with strain and compensates for the increase in the true stationary stress.

It has been seen above that both creep curves and stress strain curves are strongly affected by the back stress from the unbalanced dislocation content. In particular for creep, it was demonstrated above that the effect is huge and cannot be ignored. This is especially important to take into account in stress analysis with finite element methods (FEM). There are two straight forward alternative ways to handle the problem. The first way is to take the back stress into account explicitly. This requires however the development of special software. The other alternative is to replace the true stress σ with $\sigma \exp(-\varepsilon)$. This alternative represents no practical problem but there is a

psychological barrier because it is not in accordance with what people have been trained to do. However, ignoring it will give rise to large errors.

The dramatic effect of the back stress has only been verified for copper at lower temperatures. There are no reasons to believe that it should not applicable to other materials as well because there is nothing in the derivation that is specific for copper. The open question is to what temperature the effect survives. At a sufficiently high temperature the back stress from the unbalanced dislocations cannot be expected to be stable anymore. This section is mainly taken from [16] where further detail can be found.

8.5 Summary

- Dislocation cells are formed in virtually all alloys during plastic deformation at ambient or near ambient temperatures. Typically the cells and the surrounding cell walls are well developed after a plastic strain of about 0.3. At elevated temperatures subgrains are formed instead at least for alloys where the stacking fault energy is not too low. The subboundaries consist of thin networks of dislocations. The presence of cells or subgrains is referred to as substructure.
- Although the presence of the substructure has been discussed in many contexts in the literature, the development of substructure has only been modeled recently. Models for subgrain formation during creep and creation of cells during plastic deformation are presented in the chapter. The models can describe the limited amount of data that are available.
- During plastic deformation dislocations with opposite burgers vectors move in opposite directions in cells with the results that some parts of the cell walls have only one type of dislocations. This is referred to as unbalanced dislocations.
- The unbalanced dislocations are not exposed to static recovery since they cannot meet a dislocation of opposite sign. As a consequence the dislocation density and creep strength can continue to grow. This is believed to be the main mechanism behind the sometimes dramatic increase of the creep strength after cold work.
- The presence of unbalanced dislocations can also explain why creep curves at near ambient temperatures have a similar appearance as at much higher temperatures. The unbalanced dislocations form a massive back stress that counteracts the rapidly increasing true applied stress with increasing strain.

References

1. D.J. Michel, J. Moteff, A.J. Lovell, Substructure of type 316 stainless steel deformed in slow tension at temperatures between 21° and 816 °C. Acta Metall. **21**, 1269–1277 (1973)
2. M.E. Kassner, M.T. Pérez-Prado, Five-power-law creep in single phase metals and alloys. Prog. Mater Sci. **45**, 1–102 (2000)

3. R. Wu, N. Pettersson, Å. Martinsson, R. Sandström, Cell structure in cold worked and creep deformed phosphorus alloyed copper. Mater. Charact **90**, 21–30 (2014)
4. L. Bendersky, A. Rosen, A.K. Mukherjee, Creep and dislocation substructure. Int. Metals Rev. **30**, 1–15 (1985)
5. O.D. Sherby, R.H. Klundt, A.K. Miller, Flow stress, subgrain size, and subgrain stability at elevated temperature. Metall. Trans. A **8**, 843–850 (1977)
6. M.E. Kassner, A.K. Miller, O.D. Sherby, Separate roles of subgrains and forest dislocations in the isotropic hardening of type 304 stainless steel. Metall. Trans. A **13**, 1977–1986 (1982)
7. A. Orlová, Constitutive description of creep in polygonized substructures. Mater. Sci. Eng. A **194**, L5–L9 (1995)
8. H. Mughrabi, Dislocation wall and cell structures and long-range internal stresses in deformed metal crystals. Acta Metall. **31**, 1367–1379 (1983)
9. H. Magnusson, R. Sandstrom, The role of dislocation climb across particles at creep conditions in 9–12 pct Cr steels. Metall. Mater. Trans. A **38A**, 2428–2434 (2007)
10. S. Straub, W. Blum, D. Röttger, P. Polcik, D. Eifler, A. Borbély, T. Ungár, Microstructural stability of the martensitic steel X20CrMoV12-1 after 130000 h of service at 530 °C. Steel Res. **68**, 368–373 (1997)
11. P. Polcik, T. Sailer, W. Blum, S. Straub, J. Buršík, A. Orlová, On the microstructural development of the tempered martensitic Cr-steel P 91 during long-term creep—A comparison of data. Mater. Sci. Eng. A **260**, 252–259 (1999)
12. W. Blum, S. Straub, P. Polcik, K.H. Mayer, Quantitative investigation of microstructural evolution of two melts of the martensitic rotor steel X12CrMoWVNbN10-1-1 during long-term creep. VGB PowerTech **80**, 59–66 (2000)
13. R. Sandstrom, Subgrain growth occurring by boundary migration. Acta Metall. Mater. **25**, 905–911 (1977)
14. F. Sui, R. Sandström, Basic modelling of tertiary creep of copper. J. Mater. Sci. **53**, 6850–6863 (2018)
15. R. Sandström, The role of cell structure during creep of cold worked copper. Mater. Sci. Eng. A **674**, 318–327 (2016)
16. R. Sandström, Formation of a dislocation back stress during creep of copper at low temperatures. Mater. Sci. Eng. A **700**, 622–630 (2017)
17. D. Kuhlmann-Wilsdorf, Theory of plastic deformation: properties of low energy dislocation structures. Mater. Sci. Eng. A **113**, 1–41 (1989)
18. M.R. Staker, D.L. Holt, The dislocation cell size and dislocation density in copper deformed at temperatures between 25 and 700 °C. Acta Metall. **20**, 569–579 (1972)
19. U.F. Kocks, H. Mecking, Physics and phenomenology of strain hardening: the FCC case. Prog. Mater. Sci. **48**, 171–273 (2003)
20. D.L. Holt, Dislocation cell formation in metals. J. Appl. Phys. **41**, 3197–3201 (1970)
21. K.D. Challenger, J. Moteff, Quantitative characterization of the substructure of AISI 316 stainless steel resulting from creeP. Metall Trans **4**, 749–755 (1973)
22. V. Ganesan, M.D. Mathew, P. Parameswaran, K. Laha, Effect of nitrogen on evolution of dislocation substructure in 316LN SS during creep. Procedia Eng. **55**, 36–40 (2013)
23. D. Molnár, X. Sun, S. Lu, W. Li, G. Engberg, L. Vitos, Effect of temperature on the stacking fault energy and deformation behaviour in 316L austenitic stainless steel. Mater. Sci. Eng. A **759**, 490–497 (2019)
24. G. Meric de Bellefon, J.C. van Duysen, K. Sridharan, Composition-dependence of stacking fault energy in austenitic stainless steels through linear regression with random intercepts. J. Nucl. Mater. **492**, 227–230 (2017)
25. J.-S. Zhang, 2—Evolution of dislocation substructures during creep, in *High Temperature Deformation and Fracture of Materials* (Woodhead Publishing, 2010), pp. 14–27
26. R. Sandström, Formation of cells and subgrains and its influence on properties. Metals **12** (2022)
27. N.A. Koneva, V.A. Starenchenko, D.V. Lychagin, L.I. Trishkina, N.A. Popova, E.V. Kozlov, Formation of dislocation cell substructure in face-centred cubic metallic solid solutions. Mater. Sci. Eng. A **483–484**, 179–183 (2008)

28. V.D. Vijayanand, M. Nandagopal, P. Parameswaran, K. Laha, M.D. Mathew, Effect of prior cold work on creep rupture and tensile properties of 14Cr–15Ni–Ti stainless steel. Procedia Eng. **55**, 78–81 (2013)
29. G. Pilloni, E. Quadrini, S. Spigarelli, Interpretation of the role of forest dislocations and precipitates in high-temperature creep in a Nb-stabilised austenitic stainless steel. Mater. Sci. Eng. A **279**, 52–60 (2000)
30. J.L. Adelus, V. Guttmann, V.D. Scott, Effect of prior cold working on the creep of 314 alloy steel. Mater. Sci. Eng. **44**, 195–204 (1980)
31. T. Furuta, S. Kawasaki, R. Nagasaki, The effect of cold working on creep rupture properties for helium-injected austenitic stainless steel. J. Nucl. Mater. **47**, 65–71 (1973)
32. F. Müller, A. Scholz, C. Berger, R.-U. Husemann, Influence of cold working in creep and creep rupture behaviour of materials for super-heater tubes of modern high-end boilers and for built-in sheets in gas turbines, in *2nd International ECCC Conference. Creep & Fracture in High Temperature Components–Design & Life Assessment Issues*, ed. by S.R.H. I A Shibli (2009)
33. K.D. Challenger, J. Moteff, A correlation between strain hardening parameters and dislocation substructure in austenitic stainless steels. Scr. Metall. **6**, 155–160 (1972)
34. F. Roters, D. Raabe, G. Gottstein, Work hardening in heterogeneous alloys—A microstructural approach based on three internal state variables. Acta Mater. **48**, 4181–4189 (2000)
35. A. Argon, *Strengthening Mechanisms in Crystal Plasticity* (Oxford University Press, Oxford, 2008)
36. P. Ambrosi, C. Schwink, Slip line length of copper single crystals oriented along [100] and [111]. Scr. Metall. **12**, 303–308 (1978)
37. A.H. Delandar, R. Sandström, P. Korzhavyi, The role of glide during creep of copper at low temperatures. Metals **8** (2018)
38. H. Magnusson, R. Sandstrom, Creep strain modeling of 9–12 pct Cr steels based on microstructure evolution. Metall. Mater. Trans. A **38A**, 2033–2039 (2007)
39. R. Sandström, J. Hallgren, The role of creep in stress strain curves for copper. J. Nucl. Mater. **422**, 51–57 (2012)